J. Fluid Mech. (2024), *vol.* 998, A6, doi:10.1017/jfm.2024.888

JFM PAPERS

Inertial effects on free surface pumping with an undulating surface

Zih-Yin Chen[1], **Anupam Pandey**[2], **Daisuke Takagi**[3], **Sunghwan Jung**[4] **and Sungyon Lee**[1],†

[1]Department of Mechanical Engineering, University of Minnesota, Minneapolis, MN 55455, USA

[2]Mechanical & Aerospace Engineering Department and BioInspired Syracuse, Syracuse University, Syracuse, NY 13244, USA

[3]Department of Mathematics, University of Hawaii at Manoa, Honolulu, HI 96822, USA

[4]Department of Biological and Environmental Engineering, Cornell University, Ithaca, NY 14853, USA

(Received 25 April 2024; revised 7 August 2024; accepted 12 September 2024)

Free surface flows driven by boundary undulations are observed in many biological phenomena, including the feeding and locomotion of water snails. To simulate the feeding strategy of apple snails, we develop a centimetric robotic undulator that drives a thin viscous film of liquid with the wave speed V_w. Our experimental results demonstrate that the behaviour of the net fluid flux Q strongly depends on the Reynolds number Re. Specifically, in the limit of vanishing Re, we observe that Q varies non-monotonically with V_w, which has been successfully rationalised by Pandey *et al.* (*Nat. Commun.*, vol. 14, no. 1, 2023, p. 7735) with the lubrication model. By contrast, in the regime of finite inertia ($Re \sim O(1)$), the fluid flux continues to increase with V_w and completely deviates from the prediction of lubrication theory. To explain the inertia-enhanced pumping rate, we build a thin-film, two-dimensional model via the asymptotic expansion in which we linearise the effects of inertia. Our model results match the experimental data with no fitting parameters and also show the connection to the corresponding free surface shapes h_2. Going beyond the experimental data, we derive analytical expressions of Q and h_2, which allow us to decouple the effects of inertia, gravity, viscosity and surface tension on free surface pumping over a wide range of parameter space.

Key words: thin films, peristaltic pumping

---

† Email address for correspondence: sungyon@umn.edu

1. Introduction

The transport and manipulation of a thin liquid film arises in a wide variety of technological applications, such as coating and printing (Kalliadasis, Bielarz & Homsy 2000; Wierschem, Scholle & Aksel 2002; Decré & Baret 2003; Weinstein & Ruschak 2004), drying (Cairncross, Francis & Scriven 1996) and heat exchange processes (Das, Choi & Patel 2006). In the biological context, examples of thin-film dynamics can be found in the membranes of mammalian lungs (Grotberg 1994; Oron, Davis & Bankoff 1997) and tear films in the eye (Braun 2012).

Since the formulation of the analytical Nusselt solution (Nusselt 1916), the transport of thin films driven by gravity has been extensively studied, with the focus on the nonlinear interaction between the fluid flow and the surface wave structure (Kapitza 1948; Kapitza & Kapitza 1949; Benjamin 1957; Yih 1963; Floryan, Davis & Kelly 1987; Pozrikidis 1988; Prokopiou, Cheng & Chang 1991; Chang 1994; Liu, Schneider & Gollub 1995; Kalliadasis *et al.* 2000; Samanta 2022). By contrast, thin films driven by a peristaltic surface have begun to garner attention relatively recently, inspired by biological systems. For instance, Joo *et al.* (2020) uncovered an unusual feeding strategy of apple snails that utilise muscular undulations of their feet to drive thin, free surface flows and collect floating food particles. Motivated by this observation, Pandey *et al.* (2023) built a simple robotic undulator that generates travelling waves to pump the liquid film. Their experiments have demonstrated that the pump rate of the thin film varies non-monotonically with the speed of the undulator's travelling wave. They also built a lubrication model that successfully rationalises their experimental observations.

Despite the success of their model, the work by Pandey *et al.* (2023) solely focuses on the regime in which viscous effects dominate over inertia. However, as illustrated in gravity-driven thin films, finite inertia can drastically alter the dynamics of free surface flows, pointing to a new physical regime of interest. For instance, Malamataris, Vlachogiannis & Bontozoglou (2002) questioned the validity of the parabolic velocity profile for a flow over an inclined plane as inertia becomes non-negligible. Their analysis demonstrated that, with finite inertia, large solitary waves could develop on the free surface and also lead to the occurrence of a counterflow in the region of minimum fluid thickness. This theoretical finding was later corroborated experimentally by Tihon *et al.* (2003).

In the present manuscript, we extend the study of Pandey *et al.* (2023) to include the effects of inertia by conducting new experiments with a robotic undulator. In the experiments with non-negligible inertial effects, the pump rates show a clear deviation from the viscous-dominated regime, which cannot be explained by the original lubrication model. To explain the experimental observations, we develop a new theoretical model for the thin-film flow. To account for inertia in a mathematically tractable manner, we employ an asymptotic expansion on the velocity and pressure fields (Ruyer-Quil & Manneville 1998, 2000; Scheid, Ruyer-Quil & Manneville 2006), under the condition of a Reynolds number around $O(1)$. Similar asymptotic expansions have been previously utilised to study the effects of inertia and the effects of non-uniform surface on gravity-driven thin films (Benney 1966; Gjevik 1970; Nakaya 1975; Wang 1981). The method of expansion allows us to linearise the inertial terms in the Naiver–Stokes equation, so that we can find the analytical expressions for the velocity field and subsequently solve for fluid fluxes and free surface profiles numerically. Furthermore, we perform an additional asymptotic expansion on the free surface shape in the limit of small interfacial deformations, which yields analytical solutions of the fluid flux and gives us more precise insight into the role of inertia on free surface pumping.

Overall, our new theoretical model successfully reproduces the pump rates from the experiments with no fitting parameters, in the regimes with finite and negligible inertia. With our simplified model, we are able to more systematically probe the role of inertia, gravity and viscosity on the free surface shape, going beyond the experimental data. The analysis is able to elucidate the dependence of the free surface wave structure on the relevant non-dimensionalised numbers as well as establish the connection between the pump rate and the free surface shape. The paper is organised as follows: we introduce the experimental set-up in § 2, while the formulation of the mathematical model and the numerical method are discussed in § 3. Section 4 comprises the results of the numerical simulations in comparison with the experimental observations. In § 4.3, the analytical solutions of the fluid fluxes and the free surface profiles are provided to qualitatively rationalise the relation between free surface structures and the fluid fluxes. Finally, we conclude the paper with the summary and discussion in § 5.

2. Experiments

To create a surface with wave-like movements, we engineer an initial mechanical system depicted in figure 1(*a*). This system is identical to that of Pandey *et al.* (2023) which employs a helix's rotational motion to induce a sinusoidal travelling wave pattern on a connected surface such that the wave speed $V_w = \omega\lambda$. The helix features a constant pitch and radius which fixes the wavelength (λ) and amplitude (δ) of the travelling wave; the helix's rate of rotation is given by ω. The helix is driven by a low-power servo motor which controls ω. The helix is embedded within multiple rectangular slits which are connected by a thin ($\sim$0.1 mm) membrane. Rotation of the helix gives rise to a rhythmic undulation of this membrane forming the travelling wave. All components of this device were 3D printed with $\lambda = 50$ mm and $\delta = 2.5$ mm. On a larger length scale, an alternate method of generating a pedalling-like motion of the solid surface was demonstrated by Vivanco *et al.* (2021) who divided the bottom boundary into small elements with prescribed individual motion in an elliptical orbit.

The undulator is affixed to the bottom of a fluid-filled tank containing silicone oils (density $\rho = 970$ kg m^{-3}, viscosity $\mu = 0.97$ Pa s, interfacial tension $\sigma = 0.021$ Nm^{-1}) and glycerine–water mixtures ($\rho = 1164$ kg m^{-3}, $\mu = 0.133$ Pa s, $\sigma = 0.067$ Nm^{-1}). The depth of the liquids in the tank is maintained to such levels that only a thin layer (H) remains on top of the undulator (cf. figure 1*a*). Across all our experiments H varies between 4.3 and 8 mm which are much smaller than the wavelength of the undulations, λ. In this work, we will specifically focus on the experiments with silicone oil at $H = 6.8$ mm and water–glycerine at $H = 6.3$ mm. Travelling waves on the undulator create a directional transport of liquid within the thin film. To minimise boundary effects, we employ a spacious, acrylic tank measuring 61 cm × 46 cm.

We focus on characterising the flow rate within the thin film by performing particle image velocimetry (PIV) analysis. To this end, we introduce hollow glass particles of diameter 10 μm and illuminate these tracer particles with a 520 nm 1 Watt laser sheet. The continuous laser sheet is positioned above the liquid layer to illuminate a longitudinal plane that passes through the centre of the undulator. Then, we visualise the motion of the illuminated particles with a high-speed camera. A typical velocity field is shown in figure 1(*a*-ii), where the colour coding is based on the horizontal component of the velocity; blue is the portion of liquid with the horizontal velocity in the same direction as V_w whereas liquid in the red region has the velocity opposite to V_w.

To estimate the net transport of liquid by an undulator, we integrate the horizontal component of the fluid velocity at the mid-point of the undulator across the film thickness,

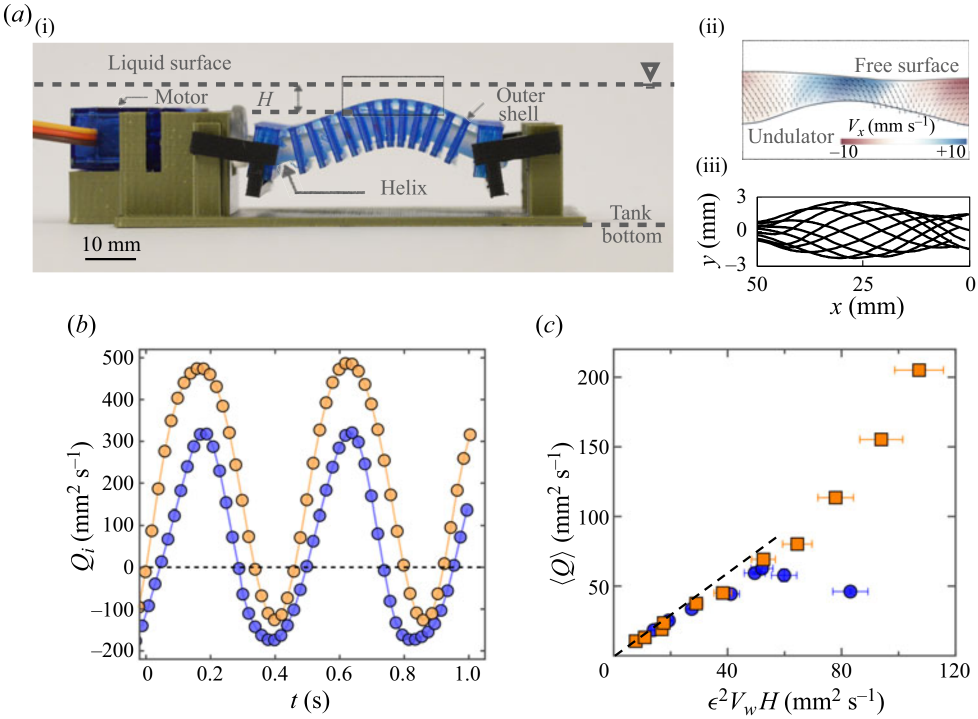

Figure 1. (*a*-i) The schematic of the robotic undulator consisting of a motor that rotates a helix encased inside a thin membrane. (*a*-ii) The PIV measurement shown with the free surface on top and the undulating solid boundary on the bottom. (*a*-iii) The undulator profile over one period of undulation. (*b*) Instantaneous flow rates Q_i as a function of time t: for silicone oil (blue) at $V_w = 90.4$ mm s^{-1} and $H = 6.8$ mm and for water–glycerine (orange) at $V_w = 78.54$ mm s^{-1} and $H = 6.3$ mm. (*c*) Time-averaged flow rate, $\langle Q \rangle$ is plotted against the wave speed V_w scaled with $\epsilon^2 H$ for silicone oil (blue) at $H = 6.8$ mm and water–glycerine (orange) at $H = 6.3$ mm. The slope of the dashed line is 1.5.

which yields an instantaneous flow rate $Q_i(t)$. Figure 1(*b*) shows the plot of $Q_i(t)$ as a function of time in silicon oil (blue) at $V_w = 90.4$ mm s^{-1} and in a water–glycerine mixture (orange) at $V_w = 78.54$ mm s^{-1}. The instantaneous flow rate fluctuates with the same time frequency as the undulator but has a positive offset. This positive offset confirms the ability of the undulator to maintain a net flow rate over a period of oscillation. Thus, we introduce a time-averaged flow rate as

$$\langle Q \rangle = \frac{1}{\tau} \int_0^\tau Q_i(t)\, \mathrm{d}t, \tag{2.1}$$

where the time scale τ is chosen to be larger than one period to avoid any end effect of sinusoidal instantaneous flow rates. Figure 1(*c*) shows the flow rate vs $\epsilon^2 V_w H$ measured in two different fluids; silicone oil (blue) at $H = 6.8$ mm and a water–glycerine mixture (orange) at $H = 6.3$ mm. The role of the geometric factor $\epsilon \equiv \delta/H$ in this plot will be clarified in the subsequent sections.

At lower values of $\epsilon^2 V_w H$ (i.e. $\lesssim 50$), $\langle Q \rangle$ is shown to increase linearly with the wave speed for both the glycerine–water mixture and silicone oil. This liquid-independent regime is a consequence of the negligible deformation of the free surface at smaller V_w and follows the relation $\langle Q \rangle = (3/2)\epsilon^2 V_w H$, as previously described by Pandey *et al.* (2023). At higher values of $\epsilon^2 V_w H$, qualitatively different behaviours are observed for the two

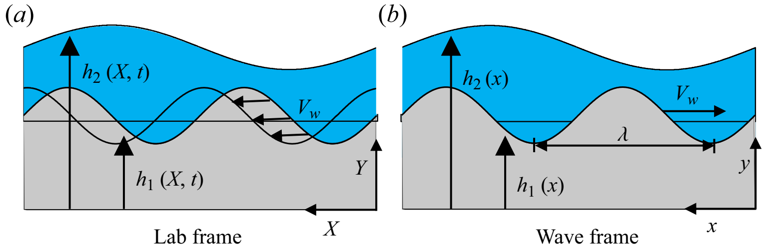

Figure 2. Schematic of a thin-film flow driven by an undulating surface with wave speed V_w and wavelength λ (*a*) in the laboratory frame and (*b*) in the wave frame. Here, the shape of solid boundary is denoted as h_1, while h_2 corresponds to the free surface profile.

liquids; while the pump rate of the silicone oil gradually increases with the wave speed, the glycerine–water mixture exhibits a non-monotonic flow rate. In the rest of the paper, we present a theoretical model that captures these different behaviours.

3. Theory

We construct a mathematical model based on the experiments. In the two-dimensional system illustrated in figure 2(*a*), we consider the flow in a film of a Newtonian liquid on an undulating boundary that undergoes a periodic deformation. The profiles of the undulating boundary and the free surface are denoted as $h_1(X, t)$ and $h_2(X, t)$, respectively, so that $h_2 - h_1$ corresponds to the thickness of the thin film. For simplicity, we model the shape of the undulating surface as $h_1(X, t) = \delta \sin[2\pi(X - V_w t)/\lambda]$, which describes the time-dependent periodic deformation with the amplitude δ, the wavelength λ and the speed of the travelling wave V_w. Consistent with the experimental set-up, the X-coordinate is defined positive in the direction of the travelling wave. We acknowledge that the actual shape generated by the robotic undulator does not follow a simple sine wave, as shown in figure 1(*a*) iii and also previously illustrated by Pandey *et al.* (2023).

To eliminate the time-dependent effects, we consider a frame moving with the wave speed V_w (Chan, Balmforth & Hosoi 2005; Lee *et al.* 2008). For the steady-state assumption to be valid, the deformation of the fluid–fluid interface and corresponding fluid flow must also move with V_w, which is qualitatively supported by the fact that the oscillation frequency of Q_i in figure 1(*b*) matches that of the undulator. We will further comment on the validity and limitation of our steady-state assumption later in this section. We use a Galilean transformation that relates the laboratory coordinates (X, Y) to the wave-frame coordinates (x, y), such that

$$x = X - V_w t, \quad y = Y. \tag{3.1a,b}$$

Thus, the transformation of the velocity field can be written as

$$u(x, y) = U(X, Y, t) - V_w, \quad v(x, y) = V(X, Y, t). \tag{3.2a,b}$$

Here, (u, v) denotes the wave-frame velocity field in the (x, y) directions, whereas (U, V) is the laboratory-frame velocity field in (X, Y) (Shapiro, Jaffrin & Weinberg 1969). Note that we first solve for the flow system in the wave frame and then convert the results back to the laboratory frame to compare with the experimental observations.

Next, we non-dimensionalise the governing equations based on the following set of characteristic scales:

$$(x, y) = \lambda(x^*, ay^*), \quad (h_1, h_2) = H(h_1^*, h_2^*), \tag{3.3a,b}$$

$$(u, v) = V_w(u^*, av^*), \quad p = p^* \mu V_w \lambda / H^2, \tag{3.4a,b}$$

where the asterisk denotes dimensionless variables, p is the gauge pressure and μ is the liquid viscosity. Note that $a \equiv H/\lambda$, where H is the mean thickness of the liquid film. In addition, the dimensionless shape of the undulating surface corresponds to $h_1^*(x^*) = \epsilon \sin(2\pi x^*)$, where $\epsilon \equiv \delta/H$. Then, the linear momentum and mass conservation equations for the fluid flow can be expressed as

$$\frac{\partial u^*}{\partial x^*} + \frac{\partial v^*}{\partial y^*} = 0, \tag{3.5}$$

$$a\widetilde{Re}\left(u^* \frac{\partial u^*}{\partial x^*} + v^* \frac{\partial u^*}{\partial y^*}\right) = -\frac{\partial p^*}{\partial x^*} + a^2 \frac{\partial^2 u^*}{\partial x^{*2}} + \frac{\partial^2 u^*}{\partial y^{*2}}, \tag{3.6}$$

$$a^3\widetilde{Re}\left(u^* \frac{\partial v^*}{\partial x^*} + v^* \frac{\partial v^*}{\partial y^*}\right) = -\frac{\partial p^*}{\partial y^*} + a^2\left(a^2 \frac{\partial^2 v^*}{\partial x^{*2}} + \frac{\partial^2 v^*}{\partial y^{*2}}\right) - \frac{Bo}{Ca}, \tag{3.7}$$

with Reynolds number $\widetilde{Re} = a\rho V_w \lambda/\mu$, Bond number $Bo = \rho g \lambda^2/\sigma$ and the capillary number $Ca = \mu V_w / a^3 \sigma$. Here, g is the gravitational acceleration. The Bo/Ca term in (3.7) corresponds to the dimensionless body force on the fluid.

The boundary conditions in the wave frame can be expressed as

$$u^* + 2\pi\epsilon a^2 \cos(2\pi x^*) v^* = -1 \quad \text{at } y^* = h_1^*, \tag{3.8}$$

$$-2\pi\epsilon \cos(2\pi x^*) u^* + v^* = 0 \quad \text{at } y^* = h_1^*, \tag{3.9}$$

$$\left[1 + a^2 \left(\frac{\partial h_2^*}{\partial x^*}\right)^2\right] \frac{\partial u^*}{\partial y^*} + 2a^2 \frac{\partial h_2^*}{\partial x^*}\left(\frac{\partial v^*}{\partial y^*} - \frac{\partial u^*}{\partial x^*}\right) + O(a^4) = 0 \quad \text{at } y^* = h_2^*, \tag{3.10}$$

$$p^* + a^2 \left(\frac{\partial h_2^*}{\partial x^*}\frac{\partial u^*}{\partial y^*} - 2\frac{\partial v^*}{\partial y^*}\right) + O(a^4) = -\frac{Ca^{-1} \dfrac{\partial^2 h_2^*}{\partial x^{*2}}}{\left[1 + a^2 \left(\dfrac{\partial h_2^*}{\partial x^*}\right)^2\right]^{3/2}} \quad \text{at } y^* = h_2^*. \tag{3.11}$$

Here, (3.8) and (3.9) correspond to the no-slip and no-flux boundary conditions on the undulator surface, respectively. On the free surface, we impose the tangential stress balance via (3.10) and the jump in normal stress due to surface tension via (3.11). For simplicity, we drop the asterisk and use ∂_x and ∂_y to denote partial differentiation with respect to the x and y coordinates in the following discussion.

Motivated by the previous studies of thin-film flows that include inertial effects (Ruyer-Quil & Manneville 1998, 2000; Scheid *et al.* 2006), we take the limit of $a \ll 1$ and apply an asymptotic expansion of the unknowns (i.e. u, v, and p) in terms of a (Roy, Roberts & Simpson 2002)

$$u(x, y) = \sum_{j=0}^{\infty} a^j u_j(x, y), \tag{3.12}$$

$$v(x, y) = \sum_{j=0}^{\infty} a^j v_j(x, y), \tag{3.13}$$

$$p(x, y) = \sum_{j=0}^{\infty} a^j p_j(x, y). \tag{3.14}$$

Following the formulation of Ruyer-Quil & Manneville (1998), we do not asymptotically expand h_2 in order of a, so that the free surface shape may include the coupled effects from all orders. In addition to $a \ll 1$, we assume that $\widetilde{Re} \sim O(1)$, which ensures that the leading inertial terms in the x-momentum equation show up at $O(a)$. Hence, our model approach is expected to fail at $\widetilde{Re} \sim O(a^{-1})$ or larger, as the linearisation of the inertial terms becomes problematic in that limit. Furthermore, at $\widetilde{Re} \gg 1$, we have experimentally observed the formation of free surface waves whose speed is distinct from the wave speed of the undulating surface. The disconnect between the two wave speeds means that our steady-state assumption in the wave frame is no longer valid. Therefore, we emphasise that the current model is valid for $\widetilde{Re} \sim O(1)$ and $a \ll 1$.

The boundary conditions also need to be decomposed to match the governing equations at each order. Note that we assume ϵ to be comparable to a. The curvature term in the normal stress boundary condition can be expanded as $\partial_{xx}h_2(1 - 3a^2(\partial_x h_2)^2/2 + O(a^4))$ by applying the binomial expansion. However, since our main purpose for the asymptotic expansion is to include the inertial effects into the model, we neglect the higher-order terms in the normal stress boundary condition and simplify (3.11) to $p = -\partial_{xx}h_2/Ca$. We acknowledge that the $O(a^2)$ term may become important in the regime where the free surface deformations are significant, which mostly falls outside our current regime of interest. Hence, we reasonably neglect the higher-order terms of the normal stress boundary condition in the rest of the discussion. The boundary conditions can be decomposed into

$$u_0 = -1, u_1 = u_2 = \cdots = 0 \quad \text{at } y = h_1, \tag{3.15}$$

$$v_0 = v_1 = v_2 = \cdots = 0 \quad \text{at } y = h_1, \tag{3.16}$$

$$\partial_y u_0 = \partial_y u_1 = \partial_y u_2 = \cdots = 0 \quad \text{at } y = h_2, \tag{3.17}$$

$$p_0 = -\partial_{xx}h_2/Ca, p_1 = p_2 = \cdots = 0 \quad \text{at } y = h_2. \tag{3.18}$$

Then, at the zeroth order, we find the following governing equations for u_0, v_0 and p_0:

$$\partial_x u_0 + \partial_y v_0 = 0, \tag{3.19}$$

$$0 = -\partial_x p_0 + \partial_{yy} u_0, \tag{3.20}$$

$$0 = -\partial_y p_0 - Bo/Ca. \tag{3.21}$$

We note that $u_0(x, y)$ is a second degree polynomial, and the solution does not include the inertial terms.

Thus, to study the inertial effects on the free surface flow, we expand the unknowns in the next two orders. Then, at $O(a^1)$, we obtain

$$\partial_x u_1 + \partial_y v_1 = 0, \tag{3.22}$$

$$\widetilde{Re}(u_0 \partial_x u_0 + v_0 \partial_y u_0) = -\partial_x p_1 + \partial_{yy} u_1, \tag{3.23}$$

$$0 = -\partial_y p_1, \tag{3.24}$$

which yield the solution of u_1 as a sixth degree polynomial of y. The equations at $O(a^2)$ correspond to

$$\partial_x u_2 + \partial_y v_2 = 0, \tag{3.25}$$

$$\widetilde{Re}(u_0 \partial_x u_1 + u_1 \partial_x u_0 + v_0 \partial_y u_1 + v_1 \partial_y u_0) = -\partial_x p_2 + \partial_{xx} u_0 + \partial_{yy} u_2, \tag{3.26}$$

$$0 = -\partial_y p_2 + \partial_{yy} v_0, \tag{3.27}$$

resulting in u_2 as a tenth degree polynomial of y. Note that both u_1 and u_2 are explicit functions of $\widetilde{Re}$. Finally, to obtain the resulting liquid flux q through the liquid layer, we integrate the velocity field in y, so that

$$q = \int_{h_1}^{h_2} \sum_{j=0}^{n} u_j(x, y)\, \mathrm{d}y. \tag{3.28}$$

Here, we replace the infinite sum in the asymptotic expansion with the partial sum up to the order n. We select $n = 2$ to provide an appropriate physical description of inertial effects with a reasonable computational cost (Ruyer-Quil & Manneville 1998, 2000). In the current wave-frame coordinates that are independent of time, conservation of mass ensures that q is constant.

Notably, q and h_2 are unknown *a priori*. Hence, we simultaneously solve for q and h_2 by imposing additional boundary conditions. As previously noted, q and h_2 are not expanded in orders of a. This enables us to numerically compute the free surface shape and fluid flux that include the effects from all orders. Based on the assumption that the undulating surface undergoes periodic deformations, we apply periodic boundary conditions for h_2 at $x = 0$ and $x = 1$. The periodic boundary conditions over each wavelength are: $h_2(0) = h_2(1)$, $\partial_x h_2(0) = \partial_x h_2(1)$, $\partial_{xx} h_2(0) = \partial_{xx} h_2(1), \ldots, \partial_{x^{n+2}} h_2(0) = \partial_{x^{n+2}} h_2(1)$ where n is the number of terms in the partial sum. In addition, we assume that the total fluid area A is conserved (i.e. $A = \int_0^1 (h_2 - h_1)\, \mathrm{d}x = 1$).

Then, the method of solving q and h_2 can be summarised as the following steps, with the details of the numerical scheme included in Appendix A:

(i) Make an initial guess for the flux q.
(ii) Find $h_2(x)$ by solving (3.28) numerically with the periodic boundary conditions.
(iii) Check the total area $A_i = \int_0^1 (h_2 - h_1)\, \mathrm{d}x$.
(iv) Change the initial guess q until the root of the function $f(q) = A - A_i$ reaches zero.

The numerical solutions of h_2 and q are presented in §§ 4.1 and 4.2. Furthermore, we obtain the analytical solution of h_2, by asymptotically expanding it in the limit of a ‘nearly flat’ surface. This allows us to derive an explicit relationship between the flux, the free surface shape and the key dimensionless parameters. The analytical results are presented in § 4.3.

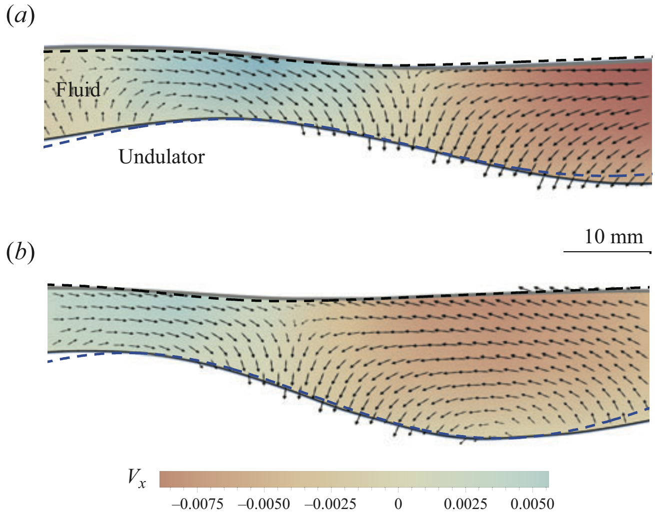

Figure 3. Results of PIV for silicone oil at $V_w = 0.0177\ \mathrm{m\ s^{-1}}$ at two different instances of time: (*a*) at $t = 0$ and (*b*) $t = 0.48$ s. The colour coding inside the thin film represents the horizontal component of the laboratory-frame velocity field that is taken to be positive in the direction of V_w. The black and the blue dashed line are the theoretical predictions of the dimensional free surface shape and the dimensional profile of the undulating boundary with (*a*) $h_1 = \sin(2\pi x)$ for $x \approx 0$–0.81 and (*b*) $h_1 = \sin(2\pi x + 0.873)$ for $x \approx 0$–0.81.

4. Results

4.1. *Comparison with experiments*

4.1.1. *Silicone oil*

We first extract the free surface shapes of silicone oil (SO) at $V_w = 0.0177\ \mathrm{m\ s^{-1}}$ and compare them with our theoretical prediction. Figure 3 shows the experimental oil–air interface in solid lines at two different times in the presence of an undulating boundary. Note that the experimental profiles are accompanied by the instantaneous PIV measurements in the laboratory frame. Figure 3 also includes the free surface shape and the undulating surface profile from our model in dashed lines. In order to compare our steady state solution with the experimental data at two different times, we have shifted our solution by an empirical offset of $\delta_{off} \approx 0.873$, such that $h_1 = \sin(2\pi x + 0.873)$ to fit the experimental image at $t = 0.48$ s. We do not expect the match between theory and experiments to be perfect, as the experimental solid boundary cannot be accurately described by a simple sine wave. We quantify the differences in h_1 and h_2 between theory and experiments by computing their L^2 norm, or $\|h_1 - h_{1\,\mathrm{exp}}\|$ and $\|h_2 - h_{2\,\mathrm{exp}}\|$, where the subscript ‘exp’ denotes the profiles from the experimental measurements. We find that $\|h_1 - h_{1\,\mathrm{exp}}\|$ and $\|h_2 - h_{2\,\mathrm{exp}}\|$ are of the same order of magnitude and are approximately 0.1 over the entire domain. Despite this discrepancy, the results in figure 3 indicate the crest of the theoretical free surface profile is slightly ahead of that of the solid boundary, which qualitatively coincides with the experimental observations.

To further delve into the free surface shapes, figure 4(*a*) shows the theoretical prediction for the free surface shapes at $V_w = 0.02$, 0.04, 0.06 and $0.08\ \mathrm{m\ s^{-1}}$. As V_w increases, the shape of the free surface gradually starts to resemble the undulating surface. The physical mechanism behind free surface deformations can be understood by comparing the dimensionless numbers in the flow system. Based on the governing equations and boundary conditions (i.e. (3.5) to (3.11)), we note that the flow system is controlled by

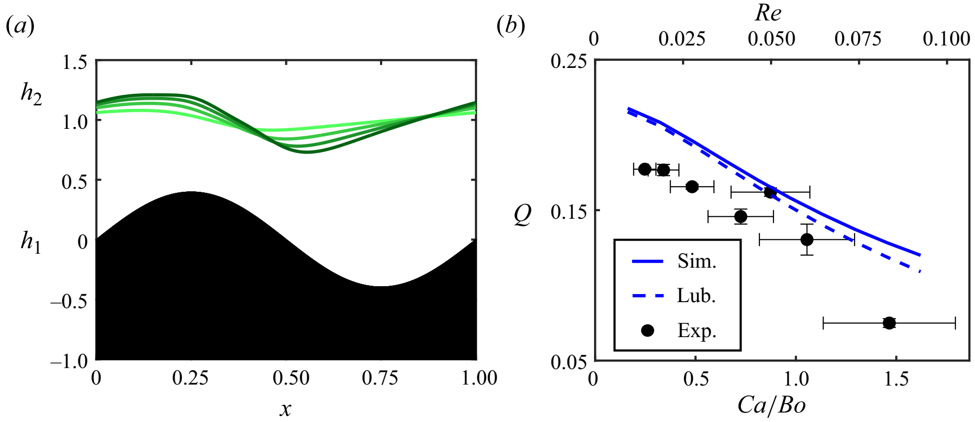

Figure 4. (*a*) The theoretical prediction of the free surface shapes for varying V_w. The different solid lines (coloured from light to dark green) correspond to the different values of $V_w = 0.02$, 0.04, 0.06 and 0.08 ms^{-1}. (*b*) The plot of laboratory-frame flux from the experiments (black dot) and theoretical predictions (blue lines) of SO. The error bars account for the uncertainty associated with the experimental measurement of H. The solid line and dashed line correspond to theoretical predictions including inertial effects (Q) and under lubrication approximations (Q_{lub}), respectively.

Re, Bo and Ca, where we have defined a modified Reynolds number $Re \equiv a\widetilde{Re}$ to account for the prefactor a in front of $\widetilde{Re}$ in (3.6). Since the magnitude of Re is around $O(10^{-2})$ as $V_w \sim O(10^{-2}\ \text{m s}^{-1})$, the inertial effect is insignificant, and the flow system is governed by Ca and Bo only. Specifically, $Ca/Bo \equiv \mu V_w/(a^3 \rho g \lambda^2)$ represents the competition between viscous and hydrostatic effects, which increases linearly with increasing V_w. Hence, for smaller V_w (or smaller Ca/Bo), a relatively flat liquid–air interface can be observed since the hydrostatic effects are dominant. By contrast, with increasing V_w (i.e. larger Ca/Bo), the free surface deformations tend to increase, which also coincides with an increase in Ca, or reduced surface tension effects.

Next, we discuss how the liquid flux varies with V_w. We propose two different theoretical predictions of the liquid flux and compare them with the experimental results. The first prediction includes inertial effects, which is equivalent to q in (3.28). The second prediction does not include inertial effect and is denoted as q_{lub}. In order to obtain q_{lub}, we follow the same procedure in § 3 but only include the terms at $O(a^0)$. Since all the inertial terms are neglected, the solution is identical to the results under lubrication approximations. However, q and q_{lub} are wave-frame fluxes, whereas the experimental results are in the laboratory frame.

To compare the theoretical predictions with the experimental results, we transform the theoretical results of the wave-frame flux into the laboratory frame by using the relation $U(X, Y, t) = u(x, y) + 1$. We find $Q_i(X_0, t) = q + (h_2(X_0, t) - h_1(X_0, t))$ by integrating the velocity from $Y = h_1(X_0, t)$ to $Y = h_2(X_0, t)$. Here, $Q_i(X_0, t)$ is the instantaneous laboratory-frame flux at a horizontal location X_0, examples of which were previously plotted in figure 1(*b*) from the PIV data. We time average Q_i based on

$$\frac{1}{\tau}\int_0^\tau Q_i(X_0, t)\,\mathrm{d}t = Q(X_0) = q + (\overline{h_2}(X_0) - \overline{h_1}(X_0)). \tag{4.1}$$

Due to the periodic nature of flow system, we note that $\overline{h_2}(X_0) - \overline{h_1}(X_0) = 1$. Since the right-hand side of (4.1) is a constant, the laboratory-frame flux Q is independent of the horizontal location X. Thus, we arrive at the following equation:

$$Q = q + 1. \tag{4.2}$$

The above transformation is also applicable under the lubrication assumption, such that $Q_{lub} = q_{lub} + 1$.

Figure 4(b) shows the experimental results of Q, plotted with the theoretical predictions of Q (solid line) and Q_{lub} (dashed line) for the range of $V_w = 0.01$–$0.1\ \mathrm{m\ s^{-1}}$. As the inertial effects are negligible (i.e. $Re \ll 1$), there are only small differences between Q_{lub} and Q, and they both effectively capture the overall decrease in the liquid flux with an increase in Ca/Bo. As V_w increases, the viscous effects gradually dominate the gravitational effects, which implies that the fluid becomes easier to undulate and move with the bottom profile, yielding a decrease in Q. However, despite the qualitative match between theory and experiments, theoretical Q tends to consistently over-predict the experimental values due to the simplified nature of our model. Specifically, the two-dimensional model cannot capture any leakage flow from the sides of the undulator, which may explain why the experimental measurements tend to be lower than the idealised model results. Finally, while the differences Q_{lub} and Q are small, Q_{lub} is systematically lower than Q as V_w is increased. This implies that the inertial effects tend to enhance the flux, which will be further explored in the next section.

4.1.2. *Glycerine–water mixture*

Next, we consider the case of choosing the glycerine–water (GW) mixture as the working liquid at $V_w = 0.023\ \mathrm{m\ s^{-1}}$. As shown in figure 5, the amplitude of the surface wave is relatively small and the free surface shape is flat for both experiments (solid lines) and theory (dashed lines). We set $h_1 = \sin(2\pi x + 0.698)$ and $h_1 = \sin(2\pi x + 2.09)$ to best match the experimental undulating boundaries in figures 5(a) and 5(b), respectively. Consistent with the results in figure 3, $\|h_1 - h_{1\,exp}\|$ and $\|h_2 - h_{2\,exp}\|$ from figure 5 are again comparable to each other and of $O(10^{-1})$. To understand the resultant free surface shape, we note that the magnitude of Ca/Bo for the GW mixture is an order of magnitude smaller than the SO case in figure 3, while the magnitude of Ca is two orders of magnitude smaller than the SO data. Hence, as the hydrostatic and surface tension effects tend to dominate in the present case, the fluid–fluid interface remains relatively flat.

Furthermore, in the experiments with the GW mixture, the magnitude of Re ranges from $O(10^{-1})$ to $O(1)$, which means that the inertial effects are no longer negligible. However, due to the dominance of Bo and the flat free surface in figure 5, the role of inertial effects remains unclear. For the following discussion, we will systematically change the wave speed to see how inertial effects may affect the free surface profile. In figure 6(a), we present the theoretical predictions of free surface profiles with $V_w = 0.03$, 0.06, 0.09 and $0.12\ \mathrm{m\ s^{-1}}$, which show that the interface deforms more as V_w increases. At the same time, the free surface gradually becomes more out of phase with the undulating surface, as more clearly illustrated in figure 6(c). The zoomed-in plot of h_2 in figure 6(c) shows that the minimum point of the free surface (denoted as a triangle) moves to the left towards the peak of the undulating substrate. This means that, distinct from the SO case, the free surface profile no longer tends to conform to the undulating surface, as the wave speed is increased.

To isolate the effects of inertia on this phenomenon, we compute and plot the free surface profiles under lubrication approximations in figure 6(b). Although the deformation of the free surface profile is insignificant compared with the SO case, it gradually changes

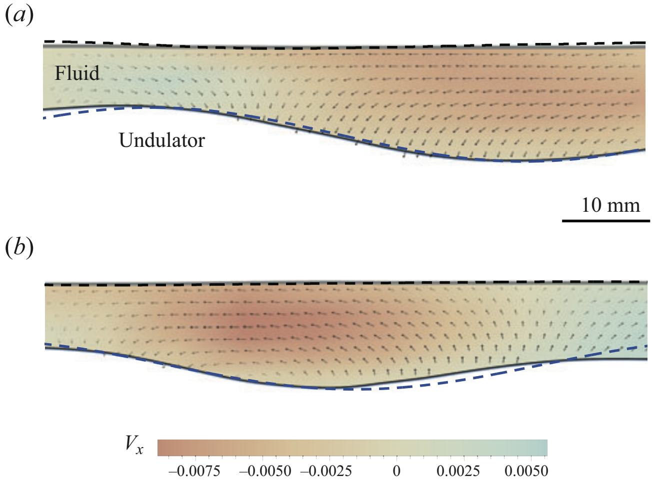

Figure 5. Results of PIV for the glycerine–water mixture at $V_w = 0.023\ \mathrm{m\ s^{-1}}$: (*a*) at $t = 0$ and (*b*) $t = 0.96\mathrm{s}$. The black and the blue dashed lines are the theoretical dimensional free surface shapes and the dimensional profiles of the undulating boundary, which are given by (*a*) $h_1 = \sin(2\pi x + 0.698)$ for $x \approx 0$–0.81, and (*b*) $h_1 = \sin(2\pi x + 2.09)$ for $x \approx 0$–0.81.

to become more in phase with h_1. This is evident in the zoomed-in plot of figure 6(*d*) that shows that the minimum point in h_2 gradually moves to the right with increasing V_w, in direct contrast to the model results in figure 6(*c*). The above observation implies two things: (i) the inertial effects enhance the amplitude of free surface deformations, and (ii) inertia causes the free surface to fall out of phase with h_1.

Next, we discuss how the free surface profile influences the fluid flux. Figure 6(*e*) shows the experimental results of Q and theoretical predictions for Q and Q_{lub} for the range of $V_w = 0.01$–$0.1\ \mathrm{m\ s^{-1}}$. We clearly observe that only the solution with the inertial effects is able to correctly capture the increase in Q with the V_w, while Q_{lub} gradually decreases with V_w. Hence, these results once again validate the role of inertia to increase the fluid flux. To connect Q to free surface shapes, we recall that inertia causes the free surface deformations to be out of phase with the lower boundary, which suggests the potential interaction between the free surface and undulating substrate. At higher Reynolds numbers, the free surface tends to form a dip towards the peak of the undulating surface. The fluid is then ‘squeezed’ by the bottom boundary and free surface that move towards each other, which, thereby, increases the liquid flux.

4.2. *The effects of Re and Ca/Bo*

While our results so far suggest that inertia enhances the fluid flux, we cannot clearly decouple the effects of inertia from viscous and hydrostatic ones, as both Re and Ca/Bo increase with V_w. To address this problem, we construct a phase map of the flux Q by varying Re and Ca/Bo independently. We first set $a = 0.126$, $H = 6.3$ mm and $\sigma = 0.02\ \mathrm{N\ m^{-1}}$ for all the simulations herein. While σ drops out of Ca/Bo, the value of σ is needed to satisfy the normal stress boundary condition at the free surface (i.e. (3.11)). In the regime with large Bo (i.e. $Bo \sim O(10^2)$–$O(10^3)$), we find that the effects of varying σ on Q are minimal and can be neglected.

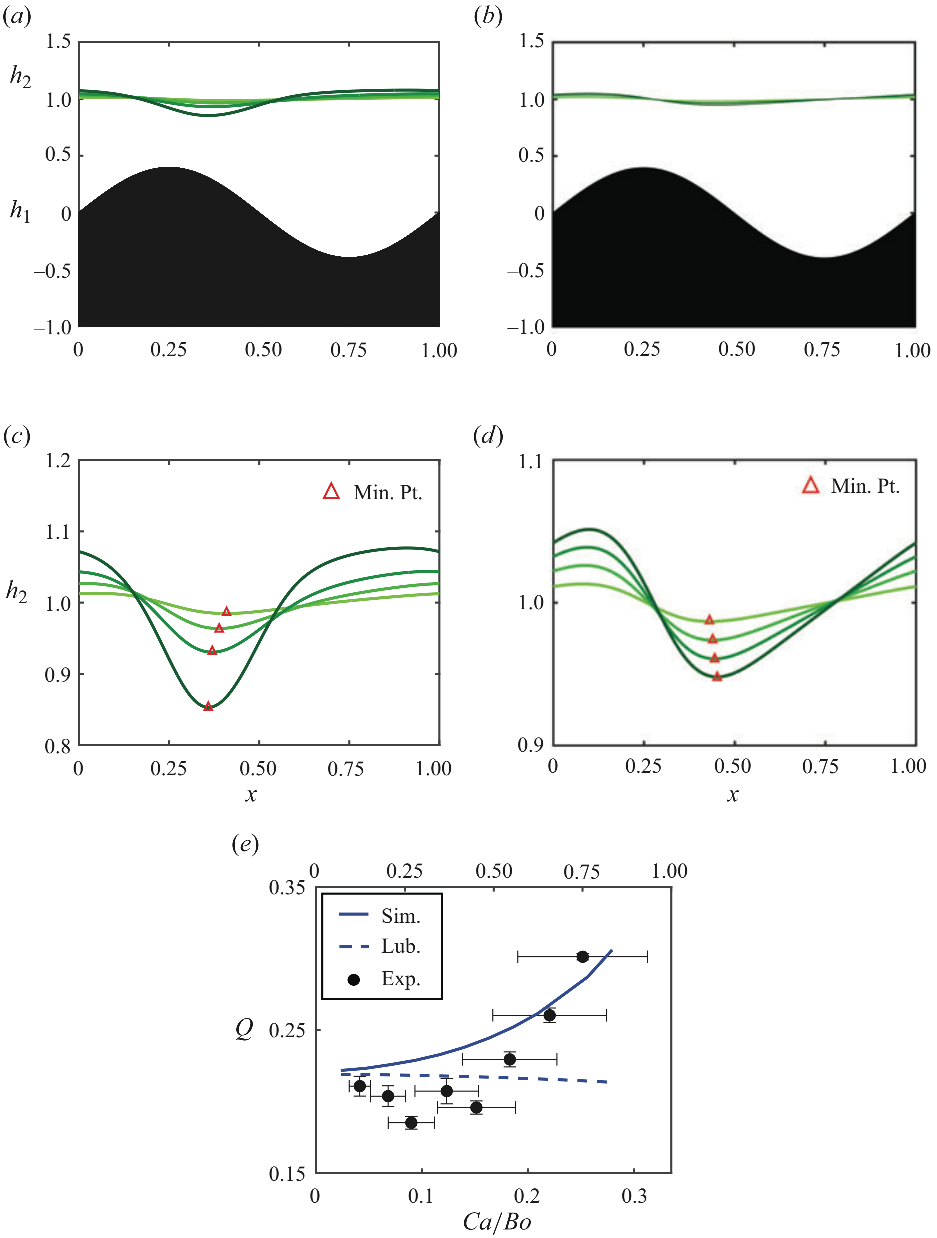

Figure 6. (*a*) The theoretical prediction of free surface shapes, where the different solid lines (coloured from light to dark green) correspond to the different values of $V_w = 0.03, 0.06, 0.09$ and $0.12\ \mathrm{m\ s^{-1}}$. (*b*) Free surface shapes under under lubrication approximation for $V_w = 0.03, 0.06, 0.09$ and $0.12\ \mathrm{m\ s^{-1}}$ (coloured from light to dark green). (*c*) The zoom-in plot of the free surface profiles from the lubrication model in (*a*); the red triangle corresponds to the minimum point in h_2. (*d*) The zoom-in plot of the free surface profiles from the lubrication model in (*b*); the red triangle corresponds to the minimum point in h_2. (*e*) The plot of laboratory-frame flux from the experiments (black dot) and theoretical predictions (blue lines) of GW. The error bars account for the uncertainty associated with the experimental measurement of H. The solid line and dashed line correspond to theoretical predictions including inertial effects (Q) and under lubrication approximations (Q_{lub}), respectively.

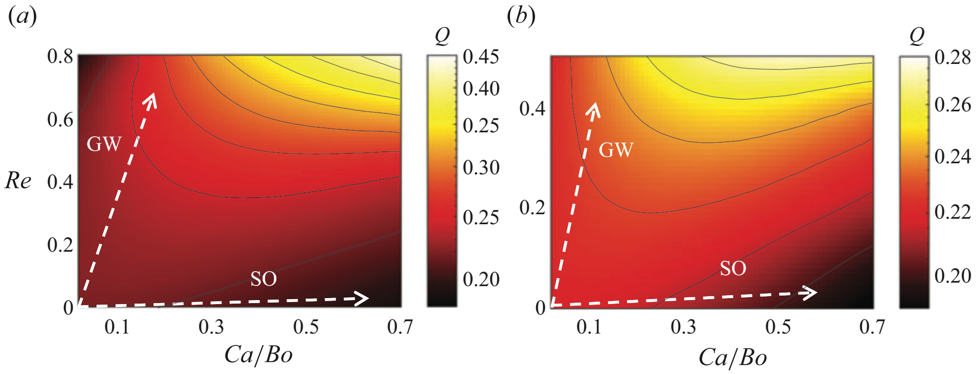

Figure 7. (*a*) Phase diagrams summarising the magnitude of Q with varying Re and Ca/Bo. The two arrows are identified as the fluid types SO and GW. The direction of the arrows corresponds to an increase in V_w. (*b*) A the zoomed-in plot of (*a*) that highlights the range of $Re = 0$–0.5. The grey contour lines correspond to constant Q.

To obtain Q at given Ca/Bo and Re, we start the simulation at $(Ca/Bo, Re) = (0.01, 0)$ and gradually increase Ca/Bo (with an increment of 0.1) and Re (with an increment of 0.1). Once the values of Q are obtained for the given range of Ca/Bo and Re, we apply a MATLAB function, *griddata* with the cubic method to interpolate our discrete simulation data and generate a smooth phase map. Notably, because Re and Ca/Bo are both linearly dependent on V_w, their ratio is independent of V_w and is given by

$$\frac{Re}{Ca/Bo} = a^2 H^3 g \left(\frac{\rho}{\mu}\right)^2, \tag{4.3}$$

where a, H and g are not fluid-dependent and remain fixed in all simulations. This implies that, once a working fluid is selected, Q for the given fluid can be represented by a straight line passing through (0, 0) with a fixed slope, where $Re/(Ca/Bo)$ corresponds to the slope.

The resulting Ca/Bo–Re phase maps of Q are shown in figure 7; the phase map in figure 7(*b*) reproduces a smaller range of Re from figure 7(*a*) for clarity. In addition, the two arrows in figure 7 correspond to the simulation results for the SO and the GW mixture, respectively. The phase maps in figure 7 reveal that Q decreases with Ca/Bo for small Re, qualitatively similar to the SO case. However, for large Re, this trend is reversed, as Q is shown to increase with Ca/Bo, with the maximum Q corresponding to the top-right corner of figure 7(*a*).

For an intermediate range for Re (i.e. $Re = 0.1$–0.5), we can clearly see in figure 7(*b*) that Q varies non-monotonically with Ca/Bo. To investigate this further, we plot Q as a function of Ca/Bo for different values of Re in figure 8. Figure 8(*a*) demonstrates that Q monotonically decreases with Ca/Bo at small Re (see blue lines) and gradually exhibits a non-monotonic behaviour with Ca/Bo as Re is increased (see green lines). Then for $Re > 0.5$, Q is shown to increase monotonically with Ca/Bo in figure 8(*b*). Hence, the effects of increasing Ca/Bo on Q are strongly dependent on Re, pointing to the potential mixed effects of Ca/Bo and Re on Q.

On the other hand, the phase diagrams in figure 7 appear to validate our earlier observation that inertia enhances the flux. To further corroborate this, we plot Q as a function of Re at constant Ca/Bo in figure 8(*c*). The main panel in figure 8(*c*) shows a monotonic increase in Q with increasing Re for Ca/Bo ranging from 0.2 to 0.8. This demonstrates positive effects of inertia on the flux. Surprisingly, at low Ca/Bo

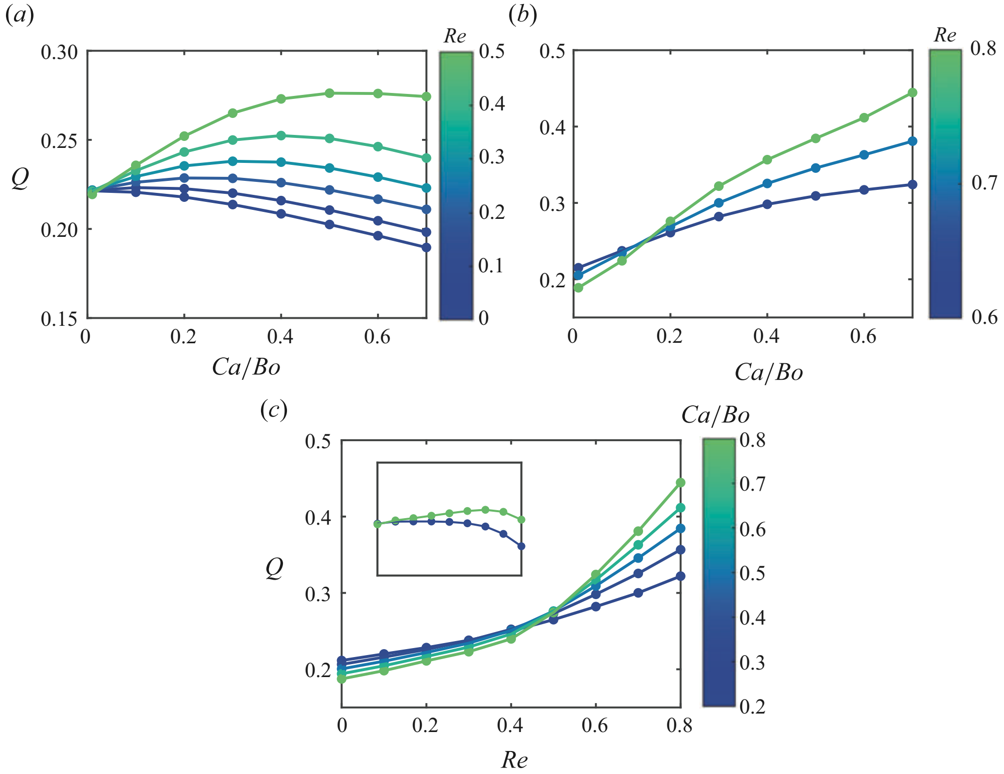

Figure 8. (*a*) The theoretical predictions of Q plotted against Ca/Bo with different values of Re from 0 to 0.5, and (*b*) from 0.6 to 0.8. (*c*) The theoretical predictions of Q plotted against Re with different values of Ca/Bo from 0.2 to 0.8. The inset shows the predictions of Q as a function of Re for $Ca/Bo = 0.01$ (blue) and 0.1 (green). The y-axis of the inset ranges from $Q = 0$ to 0.3, while the range of Re on the x-axis of the inset is the same as the main plot.

(i.e. $Ca/Bo = 0.01, 0.1$), the inset in figure 8(*c*) reveals that Q tends to decrease as Re approaches $O(1)$; this is also evident in figure 8(*b*) that shows smaller Q for larger Re near $Ca/Bo \approx 0$. This unexpected reduction in Q at relatively large Re at low Ca/Bo has two contributions. First, low Ca/Bo (i.e. large gravitational effects) ensures minimal deformation of the fluid–fluid interface, which suppresses changes in Q from the free surface shape. Second, inertia-induced changes in the velocity profile can enhance viscous dissipation from the higher-order terms, which tend to reduce Q at low Ca/Bo. Apart from this small Ca/Bo and large Re regime, increasing Re clearly enhances the overall flux. Hence, we will primarily focus on the non-monotonic behaviour of Q with Ca/Bo for non-zero Re in the next section.

Finally, the results with the SO and GW mixture in § 4.1 have demonstrated the connection between the free surface shape and the resultant flux Q. Namely, in the limit of $Re \ll 1$, increasing Ca/Bo leads to the transition of the fluid–fluid interface from flat to that conforming to the solid surface, which yields a decrease in Q. On the other hand, for $Re \sim O(0.1)$–$O(1)$, increasing Re (and Ca/Bo) causes the free surface shape to become out of phase with the undulating boundary and leads to a corresponding increase in Q.

Similar observations can be made by systematically plotting free surface shapes for varying either Re or Ca/Bo, respectively, while the other parameter is fixed. As shown in figure 9(*a*), we observe that the free surface becomes more deformed and more out of phase

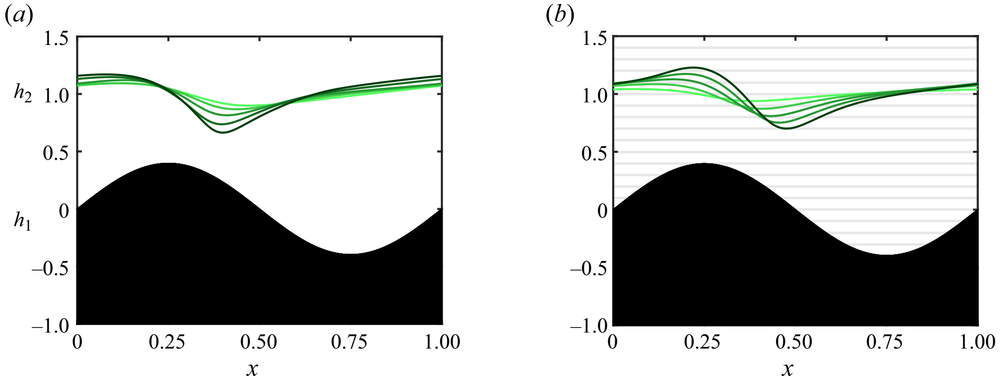

Figure 9. (*a*) The theoretical predictions of h_2 for $Ca/Bo = 0.5$ under different Re. The different solid lines (coloured from light to dark green) correspond to the values of $Re = 0$, 0.25, 0.5, 0.75 and 1. (*b*) The theoretical predictions of h_2 for $Re = 0.4$ under different Ca/Bo. The different solid lines (coloured from light to dark green) correspond to the values of $Ca/Bo = 0.2$, 0.4, 0.6, 0.8 and 1. The grey grid lines have been added to (*b*) to highlight the changes in h_2 with Ca/Bo.

with the undulating surface as we vary Re from 0 to 1 at $Ca/Bo = 0.5$. As demonstrated in figure 8(*c*), this change in the free surface shape corresponds a monotonic increase in Q, in a manner that is qualitatively similar to the GW case. By contrast, figure 9(*b*) includes the free surface shapes at $Re = 0.4$, as Ca/Bo is increased from 0.2 to 1. In this range of parameters, the free surface shape is shown to gradually evolve from flat to more in phase with the undulating surface with a larger amplitude. However, the resultant flux Q plotted in figure 8(*a*) varies non-monotonically, reaching a maximum around $Ca/Bo \approx 0.4$ before slightly decreasing with Ca/Bo. This suggests an inherent shortcoming of determining an 'optimal' free surface shape by simply plotting h_2. To help resolve the unclear connection between the free surface shape and the flux, we will derive the analytical solutions of h_2 and Q in § 4.3.

4.3. *Analytical solutions of Q and h_2*

To elucidate the mixed effects of Ca/Bo and Re, we obtain an analytical expression for Q via asymptotic expansions. First, we recall $q = q(h_1, h_2)$ via $q = \int_{h_1}^{h_2} \sum_{j=0}^{2} u_j(x, y)\,\mathrm{d}y$, which contains a term with the prefactor of Bo/Ca and that with $1/Ca$. Since the magnitude of Bo is approximately $O(10^2)$ to $O(10^3)$ based on the characteristic parameters, we neglect the term prefaced with $1/Ca$. Then, we expand q as $q = q_0 + aq_1 + a^2q_2 + a^3q_3 + O(a^4)$ by applying an asymptotic expansion of h_2 in orders of a

$$h_2 = 1 + af_1 + a^2f_2 + a^3f_3 + O(a^4). \tag{4.4}$$

In addition, q is also a function of the shape of the undulating surface, $h_1 = \epsilon \sin(2\pi x)$, where $\epsilon \equiv \delta/H$ and δ is the characteristic undulation amplitude of the solid boundary (Lee *et al.* 2008). Based on the characteristic values from the experiments, we find that a and ϵ have the same order of magnitude. Hence, we define an $O(1)$ parameter α, where $\epsilon = \alpha a$, and replace ϵ with αa to ensure that q can be consistently expanded in orders of a.

The resultant expressions of q at each order as functions of the free surface profile are listed in Appendix B, from which we solve for q_0, q_1, q_2 and q_3, together with f_1, f_2 and f_3. The analytical solutions for q_0, q_1, q_2 and q_3 and our detailed solution procedure are also included in Appendix B. Once q is known at each order, we use $Q = q + 1$

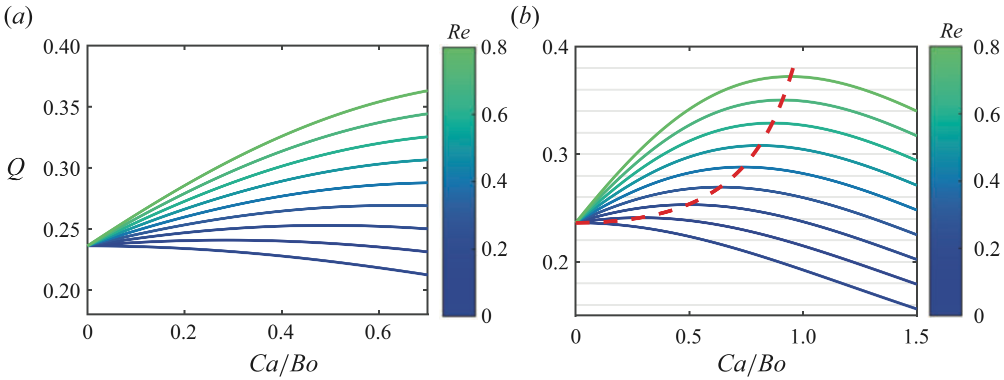

Figure 10. (*a*) The analytical solutions of Q plotted against Ca/Bo with different values of Re from 0 to 0.8. (*b*) Same asymptotic solutions with the range of Ca/Bo from 0 to 1.5, with the grey grid lines. The red dashed line depicts the maximum Q for any given Re.

(i.e. $Q_0 = 1 + q_0$, $Q_2 = q_2$ and $Q_3 = q_3$) to find the analytical expression of the laboratory-frame flux Q

$$Q = \frac{6\pi^2 a^2 \alpha^2}{9(Ca/Bo)^2 + 4\pi^2} + \frac{9a^3}{40}\alpha^2 \widetilde{Re}\left\{\frac{45(Ca/Bo)^3\pi^2 + 148(Ca/Bo)\pi^4}{(9(Ca/Bo)^2 + 4\pi^2)^2}\right\} + O(a^4), \tag{4.5}$$

where $Q_1 = 0$. We plot the first two non-zero orders of Q in (4.5) as a function of Ca/Bo for given Re, or $a\widetilde{Re}$, where $a = 0.126$. The resultant plot in figure 10(*a*) qualitatively matches the full numerical solutions of Q in figures 8(*a*) and 8(*b*) for the same parameter range. However, the asymptotic results do not exhibit the reduction in Q with increasing Re in the limit of $Ca/Bo \to 0$, as this analysis does not include the higher-order viscous terms that give rise to a slight dip in Q in this limit. As Re and $\widetilde{Re}$ simply differ by a constant prefactor, we interpret our asymptotic results in terms of Re instead of $\widetilde{Re}$ to be consistent with the results shown in figures 7 and 8.

The first term in (4.5) corresponds to $a^2 Q_2$ and only consists of Ca/Bo and monotonically decreases with increasing Ca/Bo, while the second term, $a^3 Q_3$, is the product of Re and a rational function of Ca/Bo. Specifically, for given Ca/Bo, the second term increases linearly with Re, which validates the effects of inertia to enhance the fluid flux. On the other hand, the effects of Ca/Bo on Q strongly depend on the value of Re, which helps determine the relative importance of the two terms. For instance, at $Re = 0$, only the first term is retained and leads to a decrease of Q with Ca/Bo, matching the results of the SO data.

To further elucidate the coupled effects of Re on Ca/Bo, we set $\partial Q/\partial(Ca/Bo) = 0$ to compute the critical value of Ca/Bo (i.e. Ca/Bo_{cr}) that yields the maximum value of Q at given Re. The resultant Ca/Bo_{cr} is plotted as a red dashed line in figure 10(*b*). The plots shows that Ca/Bo_{cr} monotonically increases with Re, such that $Ca/Bo_{cr} \approx 0.7$ around $Re \approx 0.4$. This explains why, in the range of Ca/Bo from 0 to 0.7, we observe the transition of Q from monotonically decreasing, being non-monotonic, then to monotonically increasing with Ca/Bo, as Re is increased (see figures 8 and 10*a*).

As shown in figure 10(*b*), once we expand the range of Ca/Bo, we can clearly observe that Q always varies non-monotonically with Ca/Bo for non-zero Re. Increasing Re simply extends the range of Ca/Bo over which Q increases, coinciding with larger Ca/Bo_{cr}. Furthermore, in the limit of $Ca/Bo \gg 1$, we find that $Q \approx (6/9)\pi^2 a^2 \alpha^2 (Ca/Bo)^{-2} +$

$(1/8)\pi^2a^3\alpha^2\widetilde{Re}(Ca/Bo)^{-1}$, which shows a monotonic decrease with Ca/Bo for all Re. Therefore, we reasonably conclude that Q is reduced in the regime where Ca/Bo dominates regardless of Re, while in the intermediate regime where Re and Ca/Bo are comparable, Q is shown to increase with Ca/Bo.

4.3.1. *Connecting free surface shapes to Q*

Going back to the asymptotic expansions in § 4.3, the free surface shape is given by $h_2 = 1 + af_1 + a^2f_2 + O(a^3)$ in response to the undulating surface of $h_1(x) = a\alpha\sin(2\pi x)$. In the limit of $a \ll 1$, we obtain the analytical expressions for f_1 and f_2 from (B3) and (B4) in Appendix B

$$f_1 = \frac{6\pi\alpha(Ca/Bo)\cos(2\pi x) + 9\alpha(Ca/Bo)^2\sin(2\pi x)}{9(Ca/Bo)^2 + (2\pi)^2}, \tag{4.6}$$

$$f_2 = 12\pi^2(Ca/Bo)\alpha\widetilde{Re}\left[\frac{12\pi(Ca/Bo)\cos(2\pi x) + (9(Ca/Bo)^2 - 4\pi^2)\sin(2\pi x)}{5(9(Ca/Bo)^2 + 4\pi^2)^2}\right] + Q_2(Ca/Bo) + F(x, Ca/Bo), \tag{4.7}$$

where $F(x, Ca/Bo)$ corresponds to

$$F = 6\pi^2\alpha^2\frac{64\pi^4 + 180\pi^2(Ca/Bo)^2 + 81(Ca/Bo)^4}{(9(Ca/Bo)^2 + 4\pi^2)^2(Ca/Bo)^2 + 16\pi^2)} + \frac{6\pi^2\alpha^2}{Bo/Ca} \times\left[\frac{9(Ca/Bo)(9(Ca/Bo)^2 - 20\pi^2)\cos(4\pi x) - 24\pi(9(Ca/Bo)^2 - 2\pi^2)\sin(4\pi x)}{(9(Ca/Bo)^2 + 4\pi^2)^2(Ca/Bo)^2 + 16\pi^2)}\right]. \tag{4.8}$$

Notably, f_1 is a linear superposition of $\cos(2\pi x)$ and $\sin(2\pi x)$, independent of Re, while f_2 comprises sine and cosine functions of higher wavenumbers and exhibits dependence on both Re and Ca/Bo. Specifically, the periodic functions with higher wavenumbers in f_2 suggest the effects of nonlinearities in our model. However, since they persist even at $\widetilde{Re} = 0$, they must stem from the nonlinearity of the free surface itself and are not related to the inertia term in the governing equation (i.e. (3.6)). On the other hand, fluid inertia from (3.6) leads to the term in f_2 that is linear in $\widetilde{Re}$. As will be further discussed, the $\widetilde{Re}$ term causes the free surface to become out of phase with h_1, which helps enhance the fluid flux.

Figure 11 includes the plots f_1 and f_2 for different dimensionless parameters; note that the dashed curve corresponds to the shape of the undulating surface, or $h_1/a = \alpha\sin(2\pi x)$, as a reference point. As shown in figure 11(*a*), f_1 is uniformly zero at $Ca/Bo = 0$ and gradually deforms more with increasing Ca/Bo. Then, as Ca/Bo reaches 10 (see the inset of figure 11*a*), f_1 closely matches the shape of the undulating surface, as the $\alpha\sin(2\pi x)$ term comes to dominates in the limit of $Ca/Bo \to \infty$.

For f_2 that depends on both Re and Ca/Bo, we first consider the effects of Ca/Bo on f_2 while Re is held constant at 0.5. Similar to the evolution of f_1, f_2 becomes more deformed as Ca/Bo is increased from 0 to 2, as shown in figure 11(*b*). However, distinct from f_1, f_2 has a flattened region near $x = 0$ that grows in amplitude with Ca/Bo, due to the contributions from constants and higher wavenumber terms in (4.8). Then, as Ca/Bo is increased above 2 (see figure 11*c*), the flat region near $x = 0$ appears to saturate and no longer grow with Ca/Bo, while the deformation of f_2 away from $x = 0$ decreases. This

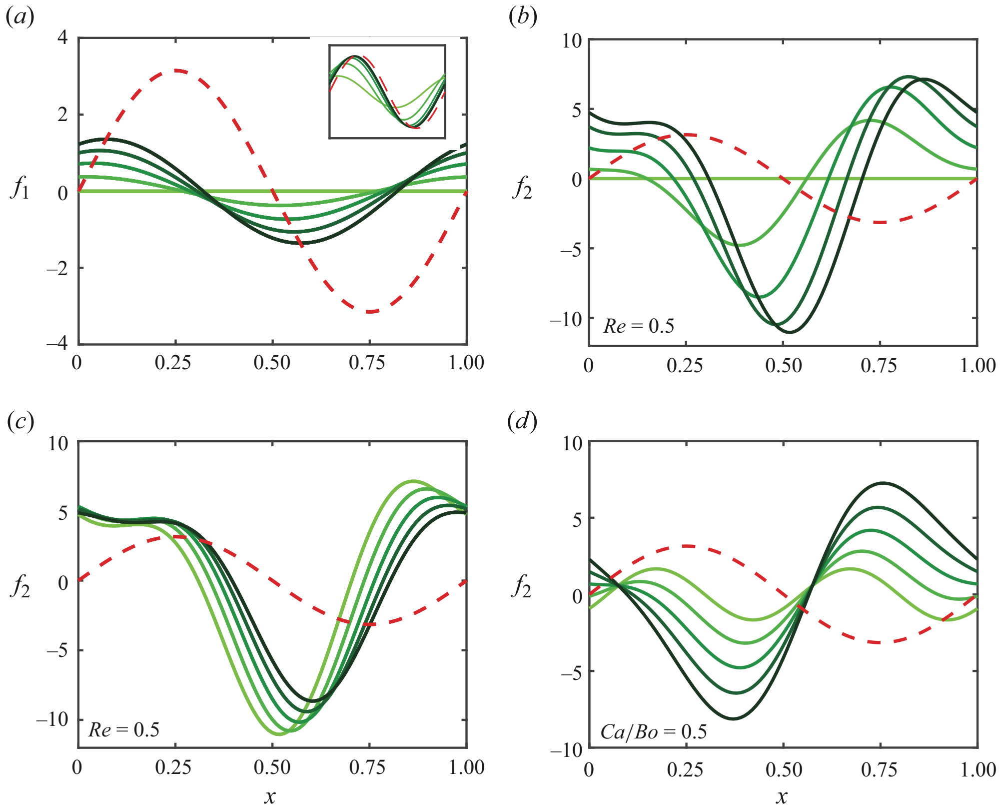

Figure 11. (*a*) The profiles of f_1 under different Ca/Bo. The different solid lines (coloured from light to dark green) correspond to the different values of $Ca/Bo = 0, 0.25, 0.5, 0.75$ and 1. The inset shows the profiles of f_1 for $Ca/Bo = 1 - 10$. (*b*) The profile of f_2 at $Re = 0.5$ for $Ca/Bo = 0, 0.5, 1, 1.5$ and 2 and (*c*) for $Ca/Bo = 2, 2.5, 3, 3.5$ and 4. (*d*) The profile of f_2 at $Ca/Bo = 0.5$ under different Re. The different solid lines (coloured from light to dark green) correspond to the different values of $Re = 0, 0.25, 0.5, 0.75$ and 1. The red-dashed lines in the figures correspond to the shape of $\alpha \sin(2\pi x)$.

non-monotonic behaviour of f_2 with Ca/Bo may have connections to the non-monotonicity in the flux Q, which will be further explored. Finally, when we instead fix Ca/Bo at 0.5 and vary Re, figure 11(*d*) shows that the wavenumber of f_2 is reduced with increasing Re, while the amplitude of deformation increases. Furthermore, f_2 becomes more out of phase with the undulating surface for increasing Re, which suggests the formation of a slight dip and a corresponding increase in Q as observed in the GW mixture case.

To more clearly understand the connection between the free surface shapes and Q, we write the resultant flux explicitly as a function of f_1 and f_2, such that

$$Q_2 = \frac{Bo}{Ca}\int_0^1 f_1'(f_1 - \alpha \sin(2\pi x))\,\mathrm{d}x, \tag{4.9}$$

$$Q_3 = \frac{Bo}{Ca}\int_0^1 [f_2'(f_1 - \alpha \sin(2\pi x)) + \widetilde{Re} f_1'(16\pi\alpha \cos(2\pi x) - 5f_1')/48 + f_1' f_2]\,\mathrm{d}x, \tag{4.10}$$

which have been reduced from (B3) and (B4) via integration (i.e. $\int_0^1 Q_2\,\mathrm{d}x = Q_2$ and $\int_0^1 Q_3\,\mathrm{d}x = Q_3$). Here, the prime denotes the differentiation with respect to x. Note that combining (4.7)–(4.10) leads to the expression for Q given in (4.5). Clearly, Q_2 scales

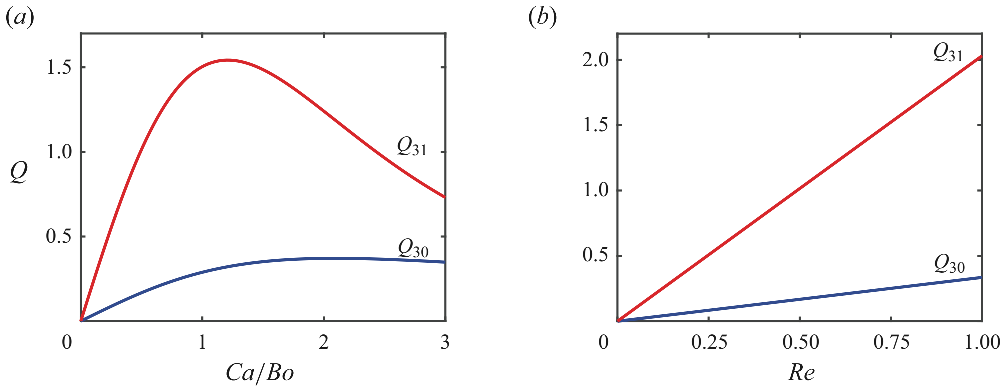

Figure 12. (*a*) Values of Q_{30} and Q_{31} plotted against Ca/Bo with $Re = 0.5$ and (*b*) Q_{30} and Q_{31} plotted against Re with $Ca/Bo = 0.5$.

with $f_1 - \alpha \sin(2\pi x)$, which explains the reduction in Q as f_1 approaches the shape of the undulating surface with increasing Ca/Bo. Furthermore, Q_2 is completely independent of Re and shows a monotonic decrease with Ca/Bo.

The effects of inertia on the flux are introduced exclusively through Q_3 in two ways: via terms that are linear in Re and those that depend on f_2. Hence, we divide up Q_3 in the following way:

$$Q_{30} = \frac{\widetilde{Re}}{48Ca/Bo}\int_0^1 f_1'(16\pi\alpha\cos(2\pi x) - 5f_1')\,\mathrm{d}x = \frac{9\pi(Ca/Bo)\alpha^2\widetilde{Re}}{72(Ca/Bo)^2 + 32\pi^2}, \tag{4.11}$$

$$Q_{31} = \frac{Bo}{Ca}\int_0^1 [f_2'(f_1 - \alpha\sin(2\pi x)) + f_1'f_2]\,\mathrm{d}x = \frac{144\pi^4(Ca/Bo)\alpha^2\widetilde{Re}}{5(9(Ca/Bo)^2 + 4\pi^2)^2}, \tag{4.12}$$

so that Q_{30} contains the effects of inertia from the changes in the flow itself, while Q_{31} includes the effects of inertia through the changes in the free surface shape via f_2. Interestingly, the higher wavenumber terms in f_2 drop out of Q_{31} upon integration, so that only inertia-induced changes in the free surface contribute to the fluid flux at $O(a^3)$.

We plot Q_{30} (blue) and Q_{31} (red) together in figure 12 as a function of Ca/Bo for $Re = 0.5$ and also for varying Re for $Ca/Bo = 0.5$, respectively. The results in figure 12 demonstrate that Q_{31} is overall larger than Q_{30}. Hence, the effects of inertia enter more strongly through the changes in the free surface shape than through the inertia-induced changes in the flow. Specifically, figure 12(*b*) shows a monotonic increase in both Q_{30} and Q_{31} for increasing Re. This increase in Q_{31} can be understood via the gradual increase in f_2 that becomes more out of phase with h_1 as Re is increased (see figure 11*d*).

By contrast, Q_{30} and Q_{31} in figure 12(*a*) show non-monotonic dependence on Ca/Bo at $Re = 0.5$, reaching a maximum at $Ca/Bo = 2\pi/3$ and $2\pi/(3\sqrt{3})$, respectively. Curiously, the transitional behaviour in f_2 as observed in figures 11(*b*) and 11(*c*) occurs around $Ca/Bo \approx 2$, which is larger than the local maximum of Q_{31} (i.e. $Ca/Bo = 2\pi/(3\sqrt{3})$). This difference in the transitional points for f_2 and Q_{31} may be explained by the fact that Q_{31} also contains a term that scales with $f_1 - \alpha\sin(2\pi x)$. As $f_1 - \alpha\sin(2\pi x)$ monotonically decreases towards zero with Ca/Bo, this term mitigates the effects of f_2 on the flux and causes Q_{31} to reach a maximum at lower Ca/Bo. Overall, we find that the changes in the flux with Re and Ca/Bo can be sufficiently explained through the corresponding changes in the free surface shape.

4.3.2. *Selection of the working fluid*

While decoupling Re and Ca/Bo is crucial in isolating the effects of inertia, in practice, we select a working fluid (i.e. ρ, μ, σ) with given film thickness H and then systematically vary V_w, which causes Re and Ca/Bo to change simultaneously. As we have experimentally demonstrated in § 4.1, once the working fluid has been selected, the resultant pump rate Q may increase or decrease with V_w, which we have rationalised in terms of Re and Ca/Bo and with corresponding free surface shapes. Building on our original experimental observations, we will discuss how the selection of working fluids determines the dependence of Q on V_w.

Going back to the phase map in figure 7, we first seek a boundary that separates Q that either increases or decreases with V_w, where the boundary satisfies the condition: $\mathrm{d}Q/\mathrm{d}V_w = 0$. In addition, we recall that Q for a given fluid can be represented by a line passing through the origin of the phase map, whose slope is given by $Re/(Ca/Bo) \propto (\rho/\mu)^2$ from (4.3). For instance, on the phase diagram in figure 7, SO corresponds to a straight line with a slope of $Re/(Ca/Bo) = 0.039$, while the GW mixture has a slope of 2.983. Hence, we will analyse how the boundary of $\mathrm{d}Q/\mathrm{d}V_w = 0$ interacts with straight lines that represent unique fluids. As the analytical solution of Q in (4.5) is a function of Re and Ca/Bo, we apply the chain rule

$$\frac{\mathrm{d}Q}{\mathrm{d}V_w} = \frac{\partial Q}{\partial Re}\frac{\partial Re}{\partial V_w} + \frac{\partial Q}{\partial (Ca/Bo)}\frac{\partial (Ca/Bo)}{\partial V_w} = 0, \tag{4.13}$$

so that

$$\begin{aligned} &\frac{9a^3\widetilde{Re}\alpha^2}{40}\left\{\frac{45(Ca/Bo)^2\pi^2 + 148\pi^4}{(9(Ca/Bo)^2+4\pi^2)^2}\right\} + \frac{9a^3\alpha^2\widetilde{Re}(135(Ca/Bo)^2\pi^2+148\pi^4)}{40(9(Ca/Bo)^2+4\pi^2)^2} \\ &\quad - \frac{108a^2\alpha^2(Ca/Bo)\pi^4}{(9(Ca/Bo)^2+4\pi^2)^2} - \frac{81a^3\alpha^2\widetilde{Re}(45(Ca/Bo)^4\pi^2+148(Ca/Bo)^2\pi^4)}{10(9(Ca/Bo)^2+4\pi^2)^3} = 0 \\ &\equiv G(\widetilde{Re}, Ca/Bo). \end{aligned} \tag{4.14}$$

We plot $G(\widetilde{Re}, Ca/Bo)$ as a dashed line in figure 13(*a*), which corresponds to the boundary of $\mathrm{d}Q/\mathrm{d}V_w = 0$. The boundary has a positive slope that monotonically increases with Ca/Bo, so the minimum slope at the origin is given by $Re/(Ca/Bo) \approx 0.164$. Therefore, a fluid with a slope smaller than 0.164 will yield Q that monotonically decreases with V_w. On the other hand, the critical slope that separates non-monotonic Q from increasing Q depends on the range of V_w considered. For instance, the critical value of $Re/(Ca/Bo)$ above which Q increases monotonically with Ca/Bo corresponds to 0.243, in the current range of Re from 0 to 1. Hence, for a fluid with $Re/(Ca/Bo)$ larger than 0.164, the behaviour of the resultant Q with V_w depends on by how much the slope exceeds 0.164 and the range of V_w considered.

To demonstrate this, in figure 13(*b*), we have plotted Q as a function of V_w for three different values of $Re/(Ca/Bo)$, representing three different fluid properties. Specifically, for a fluid whose slope is slightly higher than 0.164 (i.e. $Re/(Ca/Bo) = 0.188$), Q first increases with V_w and then begins to decrease with V_w once the line intersects $G(\widetilde{Re}, Ca/Bo)$, shown as cyan in figure 13(*b*). When $Re/(Ca/Bo)$ is set even higher at 0.243 (green line), Q monotonically increases with V_w, in a qualitatively similar manner as the GW mixture. Finally, for the fluid with $Re/(Ca/Bo) = 0.141 < 0.164$ shown in a solid blue line, Q monotonically decreases with V_w, consistent with the result of SO. Hence, we have developed a simple criterion for predicting how Q will vary with V_w based on the fluid properties and the film geometry.

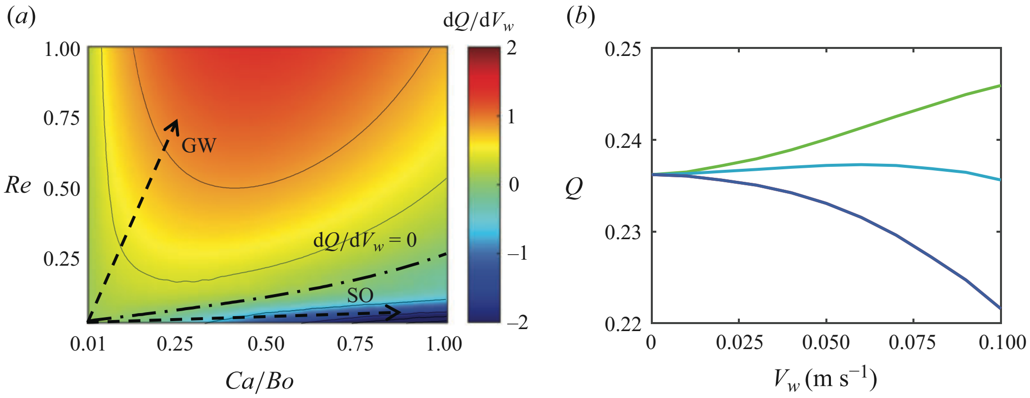

Figure 13. (*a*) The phase diagram summarising the magnitude of $\mathrm{d}Q/\mathrm{d}V_w$ with varying *Re* and *Ca*/*Bo*. The black dot-dashed line refers to $\mathrm{d}Q/\mathrm{d}V_w = 0$, with the grey contour lines corresponding to constant $\mathrm{d}Q/\mathrm{d}V_w$. (*b*) Three lines whose slopes are given by $Re/(Ca/Bo) = 0.141$ (blue), 0.188 (cyan) and 0.243 (green) exhibit distinct behaviours of Q with V_w.

5. Conclusion

In summary, we experimentally and theoretically analyse the dynamics of thin, free surface flows that are driven by an undulating surface. We experimentally demonstrate that the net pumping rate Q of the free surface flow behaves in a qualitatively different way depending on *Re*, which cannot be explained by the standard lubrication model of Pandey *et al.* (2023). To rationalise the experimental observations, we construct a two-dimensional mathematical model that incorporates the effects of finite inertia by applying an asymptotic expansion on the velocity and pressure fields. Our theoretical model correctly captures the behaviour of Q for varying wave speed V_w with no fitting parameters. The theoretical model also provides the prediction of the free surface profile for increasing V_w. Specifically, in the viscosity-dominated regime, we find that the free surface profile gradually conforms to the shape of the undulating surface and yields a decrease in Q, as observed in the experiments with SO. By contrast, in the regime with finite inertia, our model predicts that the free surface becomes out of phase with the bottom surface, which leads to a corresponding increase in Q. This is consistent with the experiments of the GW mixture.

In addition to rationalising experimental observations, we construct a phase map with numerical simulations to decouple the effects of inertia (*Re*) from viscous and hydrostatic effects (*Ca*/*Bo*). The simulation results show a decrease in Q with *Ca*/*Bo* for small *Re*, but as *Re* is increased, Q transitions to increasing with *Ca*/*Bo*, suggesting the potential mixed effects of *Ca*/*Bo* and *Re*. To further delve into these mixed effects, we derive the analytical expressions of Q and the free surface shape h_2, by expanding them in the limit of asymptotically small deformations. The resultant analytical expression of Q yields a critical value of Ca/Bo_{cr} above which Q decreases with *Ca*/*Bo*. Specifically, Ca/Bo_{cr} increases with *Re*, demonstrating that inertia tends to enhance Q and delays the dominance of the viscous effects over hydrostatics that reduce Q. We also obtain the connection between the free surface shapes h_2 and Q by analysing the analytical expressions of h_2. Finally, by setting $\mathrm{d}Q/\mathrm{d}V_w = 0$, we demonstrate how the choice of the working fluid directly influences the dependence of Q on V_w.

Overall, our two-dimensional mathematical model successfully captures the dynamics of free surface flows with an undulating surface. However, the model incorporates a number of major assumptions that could be improved upon in the future studies. For example, as *Re* is further increased, our preliminary experiments have demonstrated the generation of free surface waves that are not dictated by that of the undulating surface. Understanding this new flow regime will require bringing in the time dependence into our model, which we plan to develop in the future. In addition, due to the size of the undulator and corresponding large *Bo*, our current analysis shows negligible surface tension effects in determining the pumping rate. We hypothesise that surface tension will come to play a dominant role in the limit of small *Bo*, which we are interested in exploring with a miniaturised undulator. Finally, our future experimental studies may include adding particles on the undulator-driven free surface and exploring the effects of inertia on their trajectories (Leal 1980).

Funding. This work was partly funded by the National Science Foundation (CMMI-2042740).

Declaration of interests. The authors report no conflict of interest.

Author ORCIDs.
Anupam Pandey https://orcid.org/0000-0002-0105-3257;
Daisuke Takagi https://orcid.org/0000-0002-9738-1414;
Sunghwan Jung https://orcid.org/0000-0002-1420-7921;
Sungyon Lee https://orcid.org/0000-0002-4118-1712.

Appendix A. Numerical scheme

We first set an initial guess for the flux $q = 0.8$ (step (i)) and start the simulation with $V_w = 0.01\ \mathrm{m\ s^{-1}}$. Since the free surface deformation should be minor for small V_w, we set a flat free surface ($h_2 = 1$) as the initial guess for h_2 and use the MATLAB routine ‘bvp4c’ to compute h_2, subject to the periodic boundary conditions (step (ii)). Next, we check whether or not the total fluid area A_i for the converged solution of h_2 is conserved, or $A_i = 1$ (step (iii)). If $A_i \neq 1$, we incrementally change the value of q and repeat the process until $A_i = 1$ (step (iv)). Note that we reduce q if $A_i > 1$, whereas we increase q if $A_i < 1$. In addition, to ensure that the simulation is stable, we apply the continuation method and use the previous solution of h_2 as the initial guess, as we systematically increase V_w.

For generating the solutions as a function of Ca/Bo and *Re* (§ 4.2), we follow the same numerical scheme as described above. Specifically, to simultaneously obtain the flux and free surface shape for varying Ca/Bo, we first set the value of *Re* and start the simulation with $Ca/Bo = 0.01$ with a flat free surface ($h_2 = 1$) as the initial guess. Then, following the same steps as above, we obtain h_2 and q for systematically increasing Ca/Bo. For varying *Re*, we first fix the value of Ca/Bo and start the simulation with $Re = 0.01$. However, the initial profile of h_2 is not set to be flat for large Ca/Bo. Instead, we replace $h_2 = 1$ with $(h_2, h_2', h_2'', h_2''', h_2'''', h_2''''') = (1, 0.1, 0, 0, 0)$ and change the last three guesses with small adjustments (e.g. 0.01), to obtain the converged solution of h_2 via ‘bvp4c’ if necessary.

Appendix B. Asymptotic expansions of q

Expanding q via the asymptotic expansion of h_2 yields the following expressions for q_0, q_1, q_2 and q_3:

$$q_0 = -1, \tag{B1}$$

$$q_1 = -f_1 + \alpha \sin(2\pi x) - \frac{1}{3Ca/Bo} f_1', \tag{B2}$$

$$q_2 = -f_2 - \frac{1}{Ca/Bo} f_1 f_1' + \frac{\alpha}{Ca/Bo}\sin(2\pi x) f_1' + \frac{1}{3Ca/Bo} f_2' - \frac{\widetilde{Re}}{15Ca/Bo} f_1'', \tag{B3}$$

$$\begin{aligned} q_3 = {} & -f_3 + \frac{\pi\alpha\widetilde{Re}}{3Ca/Bo}\cos(2\pi x) f_1' - \frac{1}{Ca/Bo} f_1'(f_1^2 - f_2) + \frac{2\alpha}{Ca/Bo}\sin(2\pi x) f_1 f_1'' \\ & - \frac{\alpha^2}{Ca/Bo}\sin^2(2\pi x) f_1 \frac{5\widetilde{Re}}{48Ca/Bo} f_1'^2 - \frac{1}{Ca/Bo} f_1 f_2' + \frac{\alpha}{Ca/Bo}\sin(2\pi x) f_2' - \frac{1}{3Ca/Bo} f_3' \\ & - \frac{\widetilde{Re}}{3Ca/Bo} f_1 f_1'' + \frac{\widetilde{Re}\alpha}{3Ca/Bo}\sin(2\pi x) f_1'' - \frac{37\widetilde{Re}\alpha}{1680(Ca/Bo)^2} f_1' f_1'' - \frac{\widetilde{Re}}{15Ca/Bo} f_2'' \\ & - \frac{1}{40Ca/Bo} f_1''' - \frac{17\widetilde{Re}^2}{1260Ca/Bo} f_1'''. \end{aligned} \tag{B4}$$

We note that $q_0 = -1$ as a consequence of being in the wave frame.

Next, we simultaneously solve for q and f at each order via the 'DSolve' function in Mathematica, by imposing the periodic boundary conditions and the conservation of fluid area. Note that $\int_0^1 (h_2 - h_1)\,\mathrm{d}x = 1$ can be simplified to $\int_0^1 h_2\,\mathrm{d}x = 1$, since $h_1 = \alpha a \sin(2\pi x)$. Also, the first term in the expansion of h_2 is 1, which automatically satisfies the total fluid area. Hence, the conservation of fluid area for the remaining terms in the expansion becomes $\int_0^1 f_n\,\mathrm{d}x = 0$ for $n = 1, 2, 3$. The resultant analytical solutions for q_1, q_2 and q_3 correspond to

$$q_1 = 0, \tag{B5}$$

$$q_2 = \frac{6\pi^2\alpha^2}{9(Ca/Bo)^2 + 4\pi^2}, \tag{B6}$$

$$q_3 = \frac{9\widetilde{Re}(45\pi^2(Ca/Bo)^3 + 148\pi^4(Ca/Bo))}{40(9(Ca/Bo)^2 + 4\pi^2)^2}. \tag{B7}$$

REFERENCES

BENJAMIN, T.B. 1957 Wave formation in laminar flow down an inclined plane. *J. Fluid Mech.* **2** (6), 554–573.

BENNEY, D.J. 1966 Long waves on liquid films. *J. Maths Phys.* **45** (1-4), 150–155.

BRAUN, R.J. 2012 Dynamics of the tear film. *Annu. Rev. Fluid Mech.* **44**, 267–297.

CAIRNCROSS, R.A., FRANCIS, L.F. & SCRIVEN, L.E. 1996 Predicting drying in coatings that react and gel: drying regime maps. *AIChE J.* **42** (1), 55–67.

CHAN, B., BALMFORTH, N.J. & HOSOI, A.E. 2005 Building a better snail: lubrication and adhesive locomotion. *Phys. Fluids* **17** (11), 113101.

CHANG, H.-C. 1994 Wave evolution on a falling film. *Annu. Rev. Fluid Mech.* **26** (1), 103–136.

DAS, S.K., CHOI, S.U. & PATEL, H.E. 2006 Heat transfer in nanofluids – a review. *Trans. ASME Heat Transfer Engng* **27** (10), 3–19.

DECRÉ, M.M.J. & BARET, J.-C. 2003 Gravity-driven flows of viscous liquids over two-dimensional topographies. *J. Fluid Mech.* **487**, 147–166.

FLORYAN, J.M., DAVIS, S.H. & KELLY, R.E. 1987 Instabilities of a liquid film flowing down a slightly inclined plane. *Phys. Fluids* **30** (4), 983–989.

GJEVIK, B. 1970 Occurrence of finite-amplitude surface waves on falling liquid films. *Phys. Fluids* **13** (8), 1918–1925.

GROTBERG, J.B. 1994 Pulmonary flow and transport phenomena. *Annu. Rev. Fluid Mech.* **26** (1), 529–571.

JOO, S., JUNG, S., LEE, S., COWIE, R.H. & TAKAGI, D. 2020 Freshwater snail feeding: lubrication-based particle collection on the water surface. *J. R. Soc. Interface* **17** (165), 20200139.

KALLIADASIS, S., BIELARZ, C. & HOMSY, G.M. 2000 Steady free-surface thin film flows over topography. *Phys. Fluids* **12** (8), 1889–1898.

KAPITZA, P.L. 1948 Wave flow of thin layers of a viscous fluid: II. Fluid flow in the presence of continuous gas flow and heat transfer. *Zh. Eksp. Teor. Fiz.* **18** (19), 680–689. Also in Collected Papers of P. L. Kapitza (ed. D. Ter Haar), pp. 690–709. Pergamon, 1965.

KAPITZA, P.L. & KAPITZA, S.P. 1949 Wave flow of thin fluid layers of liquid. *Zh. Eksp. Teor. Fiz.* **19**, 105, also in Collected Papers of P. L. Kapitza (ed. D. Ter Haar), pp. 690–709. Pergamon, 1965.

LEAL, L.G. 1980 Particle motions in a viscous fluid. *Annu. Rev. Fluid Mech.* **12** (1), 435–476.

LEE, S., BUSH, J.W.M., HOSOI, A.E. & LAUGA, E. 2008 Crawling beneath the free surface: water snail locomotion. *Phys. Fluids* **20** (8), 082106.

LIU, J., SCHNEIDER, J.B. & GOLLUB, J.P. 1995 Three-dimensional instabilities of film flows. *Phys. Fluids* **7** (1), 55–67.

MALAMATARIS, N.A., VLACHOGIANNIS, M. & BONTOZOGLOU, V. 2002 Solitary waves on inclined films: flow structure and binary interactions. *Phys. Fluids* **14** (3), 1082–1094.

NAKAYA, C. 1975 Long waves on a thin fluid layer flowing down an inclined plane. *Phys. Fluids* **18** (11), 1407–1412.

NUSSELT, W. 1916 Die oberflachenkondensation des wasserdamphes. *VDI-Zs* **60**, 541.

ORON, A., DAVIS, S.H. & BANKOFF, S.G. 1997 Long-scale evolution of thin liquid films. *Rev. Mod. Phys.* **69** (3), 931.

PANDEY, A., CHEN, Z.-Y., YUK, J., SUN, Y., ROH, C., TAKAGI, D., LEE, S. & JUNG, S. 2023 Optimal free-surface pumping by an undulating carpet. *Nat. Commun.* **14** (1), 7735.

POZRIKIDIS, C. 1988 The flow of a liquid film along a periodic wall. *J. Fluid Mech.* **188**, 275–300.

PROKOPIOU, T., CHENG, M. & CHANG, H.-C. 1991 Long waves on inclined films at high Reynolds number. *J. Fluid Mech.* **222**, 665–691.

ROY, R.V., ROBERTS, A.J. & SIMPSON, M.E. 2002 A lubrication model of coating flows over a curved substrate in space. *J. Fluid Mech.* **454**, 235–261.

RUYER-QUIL, C. & MANNEVILLE, P. 1998 Modeling film flows down inclined planes. *Eur. Phys. J.* B-*Condens. Matter Complex Syst.* **6** (2), 277–292.

RUYER-QUIL, C. & MANNEVILLE, P. 2000 Improved modeling of flows down inclined planes. *Eur. Phys. J.* B-*Condens. Matter Complex Syst.* **15** (2), 357–369.

SAMANTA, A. 2022 Role of odd viscosity in falling viscous fluid. *J. Fluid Mech.* **938**, A9.

SCHEID, B., RUYER-QUIL, C. & MANNEVILLE, P. 2006 Wave patterns in film flows: modelling and three-dimensional waves. *J. Fluid Mech.* **562**, 183–222.

SHAPIRO, A.H., JAFFRIN, M.Y. & WEINBERG, S.L. 1969 Peristaltic pumping with long wavelengths at low Reynolds number. *J. Fluid Mech.* **37** (4), 799–825.

TIHON, J., TOVCHIGRECHKO, V., SOBOLIK, V. & WEIN, O. 2003 Electrodiffusion detection of the near-wall flow reversal in liquid films at the regime of solitary waves. *J. Appl. Electrochem.* **33** (7), 577–587.

VIVANCO, I., CARTWRIGHT, B., LEDESMA ARAUJO, A., GORDILLO, L. & MARIN, J.F. 2021 Generation of gravity waves by pedal-wavemakers. *Fluids* **6** (6), 222.

WANG, C.-Y. 1981 Liquid film flowing slowly down a wavy incline. *AIChE J.* **27** (2), 207–212.

WEINSTEIN, S.J. & RUSCHAK, K.J. 2004 Coating flows. *Annu. Rev. Fluid Mech.* **36**, 29–53.

WIERSCHEM, A., SCHOLLE, M. & AKSEL, N. 2002 Comparison of different theoretical approaches to experiments on film flow down an inclined wavy channel. *Exp. Fluids* **33** (3), 429–442.

YIH, C.-S. 1963 Stability of liquid flow down an inclined plane. *Phys. Fluids* **6** (3), 321–334.